Supplementary Information (SI) for Journal of Materials Chemistry A.

Supporting Information

Controlled synthesis and interfacial properties of polyvinylidene fluoride based metal-fluoride surface treatments for high-nickel NCM cathodes

HeeSang Lee,†[a] Wonchan Hwang,†[b] Jahun Koo,†[a] Hendrik Ohldag,[c] David A. Shapiro,[c] Eun-Jung Shin,[d] Min-Su Kim,[d] Moonjung Jung,[e] Namdong Kim,[e] Jungjin Park,*[b] Young-Sang Yu*[df] and Chunjoong Kim*[a]

[a] Department of Materials Science and Engineering, Chungnam National University, Daejeon 34134, Republic of Korea

[b] Energy Storage Research Center, Korea Institute of Science and Technology (KIST), Seoul 02792, Republic of Korea

[c] Advanced Light Source, Lawrence Berkeley National Laboratory, Berkeley, CA 94720, USA

[d] Department of Physics, Chungbuk National University, Cheongju 28644, Republic of Korea

[e] Pohang Accelerator Laboratory, Pohang University of Science and Technology, Pohang 37673, Republic of Korea

[f] Advanced Energy Research Institute, Chungbuk National University, Cheongju 28644, Republic of Korea

† H.L., W.H., and J. K. contributed equally to this work.

*Corresponding authors

E-mail addresses: jpark716@kist.re.kr (J. Park), youngsang@chungbuk.ac.kr (Y.-S. Yu), ckim0218@cnu.ac.kr (C. Kim)

S1. Preparation of metal-fluoride-coated high-Ni NCM active material

The precursor, $Ni_{0.960}Co_{0.035}Mn_{0.005}(OH)_2$, was prepared using a co-precipitation method. A 1.5 M aqueous solution containing nickel sulfate hexahydrate ($NiSO_4 \cdot 6H_2O$, Samchun Chemical, Korea), cobalt sulfate heptahydrate ($CoSO_4 \cdot 7H_2O$, Samchun Chemical, Korea), and manganese sulfate monohydrate ($MnSO_4 \cdot H_2O$, Samchun Chemical, Korea) in a 96.0:3.5:0.5 molar ratio was used as the source of TMs. 4 M sodium hydroxide (NaOH, Samchun Chemical, Korea) served as both the reducing agent and pH adjuster, while ammonia (NH_3, Samchun Chemical, Korea) with a constant concentration of 1 M acts as a chelating agent and retards the reaction. The co-precipitation reaction was conducted for 20 hours at a pH of 11.2. The TM sulfate solution was continuously fed into the reactor at a rate of 80 mL h^{-1} under an N_2 atmosphere. The precursor, $Ni_{0.960}Co_{0.035}Mn_{0.005}(OH)_2$, was filtered and washed with deionized water (DI) to remove any residual ions, then dried at 80 °C overnight. The NCM active material was synthesized by mixing the precursor and lithium hydroxide ($LiOH \cdot H_2O$, Junsei Chemical) in a 1:1.02 molar ratio. The mixed powder was preheated at 400 °C for 2 h and subsequently calcined at 710 °C for 12 h. All heat treatment steps were carried out in an oxygen atmosphere to ensure proper material formation. A schematic illustration of the fluorine coating method applied to fully synthesized high-Ni NCM using PVDF is presented in **Fig. S1**. The NCM active material was mixed with 1 wt.% PVDF ($-(C_2H_2F_2)_n-$, solef 6020, Solvay) in acetone, then dried at 60 °C for the complete evaporation of the solvent. For comparison, the PVDF content was increased to 3 and 5 wt.% for the control samples. The mixed powder was then pelletized at approximately 27 MPa for 5 min to promote intimate physical contact between solid states. The obtained pellets were heat-treated at 350 °C under an argon atmosphere to decompose PVDF and substitute surface oxygen sites with fluoride.

S2. Electrochemical tests

The 2032-type coin half-cells were assembled using lithium metal (anode), high-Ni NCM (cathode), and an electrolyte consisting of 1 M $LiPF_6$ dissolved in a solvent mixture of ethylene carbonate (EC), dimethyl carbonate (DMC), and ethyl methyl carbonate (EMC) in a 1:1:1 volumetric ratio. Cathodes were prepared from a mixture of either uncoated or fluorine-coated (F-coated) high-Ni NCM secondary powder, acetylene black (Denka) as the conductive additive, and PVDF (Sigma Aldrich) as the binder in an 8:1:1 weight ratio. The powder mixture was dissolved in N-methyl-2-pyrrolidone (NMP) and homogenized by a mixing machine (Inter-Mixer IMX-150, KM Tech). The slurry mixture was uniformly spread to an approximate thickness of 40 μm on 20-μm-thick aluminium foils (current collector) using a doctor blade film applicator. The anode, cathode, and monolayer polypropylene (PP) separator (Celgard 2400) were punched into disk shapes with a diameter of 14 mm to match the dimensions of the 2032-type coin cell. The electrochemical performance of both uncoated and F-coated NCMs was tested under various temperatures and cut-off voltages. To verify the enhanced performance resulting from the fluorine coating, electrochemical tests, including capacity retention rate assessments, were conducted at an elevated temperature of 40 ^{o}C and over a wide potential range from 2.7 to 4.5 V, which represent the extreme oxygen reduction conditions within the host structure. Electrochemical impedance spectroscopy (EIS) measurements were conducted over a frequency range from 10^6 to 10^{-3} Hz. The Li^+ diffusion coefficient (D_{Li+}) was calculated from the Warburg coefficient obtained from the low-frequency region of the impedance spectra, using the parameters T = 293.15 K and electrode area S = 1.59 cm^2. The Li^+ concentration (C) was calculated based on the layered $R\bar{3}m$ structure as an approximation. In addition, Li^+ ion diffusivity was evaluated by GITT at each voltage during charge/discharge (current density = 20 mA g^{-1}, pulse duration = 600 s). During repeated GITT intercalation and deintercalation steps, the cells were allowed to rest for 2400 s after each step until cut-off potentials of 2.7 V or 4.5 V were reached. The extent of surface-induced amorphous rock-salt NiO formation was comparatively analyzed. The Li$^+$ ion diffusivity was calculated at each voltage after charge/discharge using GITT (current density = 20 mA g^{-1}, pulse duration = 600 s), and the extent of surface-induced amorphous rock-salt NiO formation was comparatively analyzed. During repeated GITT intercalation and deintercalation steps, the cells were allowed to rest for 2400 s after each step until cut-off potentials of 2.7 V or 4.2 V were reached. The GITT test was applied to each active material every 10 cycles. Assuming a spherical particle radius of r_P = 7.8 μm, the lithium-ion diffusivity in the active material was calculated by following equation (**Fig. S10**) [1]

$$D = \frac{4}{9\pi} \cdot \left(\frac{E_4 - E_0}{E_3 - E_0}\right)^2 \cdot \frac{r_P^2}{t_P}$$

The capacity-matched cycling tests were performed using four independent 2032-type half-cells for each sample. After the formation cycle, the first-cycle discharge capacities were examined, and a common charge-capacity limit of 205 mAh g^{-1} was selected based on the minimum discharge capacity observed among all tested cells. From the second cycle onward, both uncoated and F-coated NCM electrodes were cycled under the same operating conditions used in the main manuscript, except that the charge capacity was limited to 205 mAh g^{-1}. Charging was carried out at 200 mA g^{-1} in CCCV mode within 2.7-4.5 V with a cut-off current of 10 mA g^{-1}, and discharge was performed at 200 mA g^{-1} in CC mode down to 2.7 V for 50 cycles. Under this protocol, all cells reached the upper cut-off voltage of 4.5 V during charging, confirming that both electrodes were evaluated in the same high-voltage regime while maintaining an equivalent amount of Li extraction. The corresponding capacity-matched cycling results are presented in **Fig. S9**.

S3. STXM analysis of chemical states and elemental distribution

To investigate the surface chemistry on F-coated NCM, STXM was utilized to measure two-dimensional image spectra, which is the systematic acquisition of repeated X-ray transmission images, each captured at sequentially varied incident photon energies. The analysis was carried out on the elliptically polarizing undulator beamline (Beamline 11.0.2.2) at the Advanced Light Source, Lawrence Berkeley National Laboratory [2, 3]. The incident photon energy, particularly near the fluorine *K*-edge, was precisely calibrated by comparing the absorption features of reference gases (CO_2 and Ne) and a metallic thin film (an Fe/Gd multilayer protected against oxidation by a Ta capping layer) with tabulated data [4]. The primary particles, obtained by fragmenting secondary particles via high-power sonication, were drop-cast onto copper grids coated with X-ray-transparent carbon thin films (01843, Ted Pella, Inc.). To detect infrequently occurring primary particles with fluorine, a comprehensive examination of several hundred primary particles was conducted by utilizing a two-energy difference map, which compared one absorption image from the pre-edge region and another from white-line energy. For the chosen primary particles, the image spectra were acquired across the F *K*-edge, yielding spatial sensitivity with either 25 or 40 nm pixel size, varying based on the sample size and acquisition time. The most precise energy increment was 0.25 eV near the absorption resonance features. Based on Beer's law, the transmitted X-ray intensities at each raster point were transformed into optical density (OD). Subsequently, these OD images underwent precise alignment with sub-pixel accuracy, employing an iterative registration algorithm to compensate for spatial variations in spectral information [5]. The chemical state of the fluorine content was analyzed by comparing it with reference spectra for lithium fluoride (LiF) and PVDF [6, 7].

Additional STXM analyses were performed at the 10A1 beamline of Pohang Light Source II (PLS-II) [8] using focused ion beam (FIB, Helios G4, FEI)-milled lamellae prepared from pristine F-coated NCM secondary particles. Each lamella was thinned to approximately 150 nm to ensure sufficient soft X-ray transmission near the O *K*-, F *K*-, and Ni *L*-edges. Spectral image stacks, i.e., sequentially acquired transmission maps across the O, F, and Ni absorption edges, were collected by raster scanning with a step size of 40 nm and a dwell time of 2 ms. The smallest energy increment was 0.25 eV near the absorption resonance features. The transmission images underwent the same image-processing procedure used for the 11.0.2.2 beamline data, including OD conversion and image registration. The Ni oxidation-state maps were quantitatively determined by linear-combination fitting of the reference spectra for Ni^{2+} from $LiMn_{1.5}Ni_{0.5}O_4$ spinel and Ni^{3+} from $LiNi_{0.8}Co_{0.15}Al_{0.05}O_2$, as shown in **Fig. S5**. The quality of the linear-combination fitting at each pixel was evaluated using the *R*-factor $\left(= \frac{\sum_{i} (Data - Fit)^2}{\sum_{i} (Data)^2} \right)$, and pixels with *R*-factors greater than 0.10 were excluded from further quantification. The boundaries of the thinned secondary particles were determined from the OD image acquired at 854 eV (**Fig. 2a**) using a combination of global thresholding based on Otsu's method [9] and an OD intensity contour-tracing procedure.

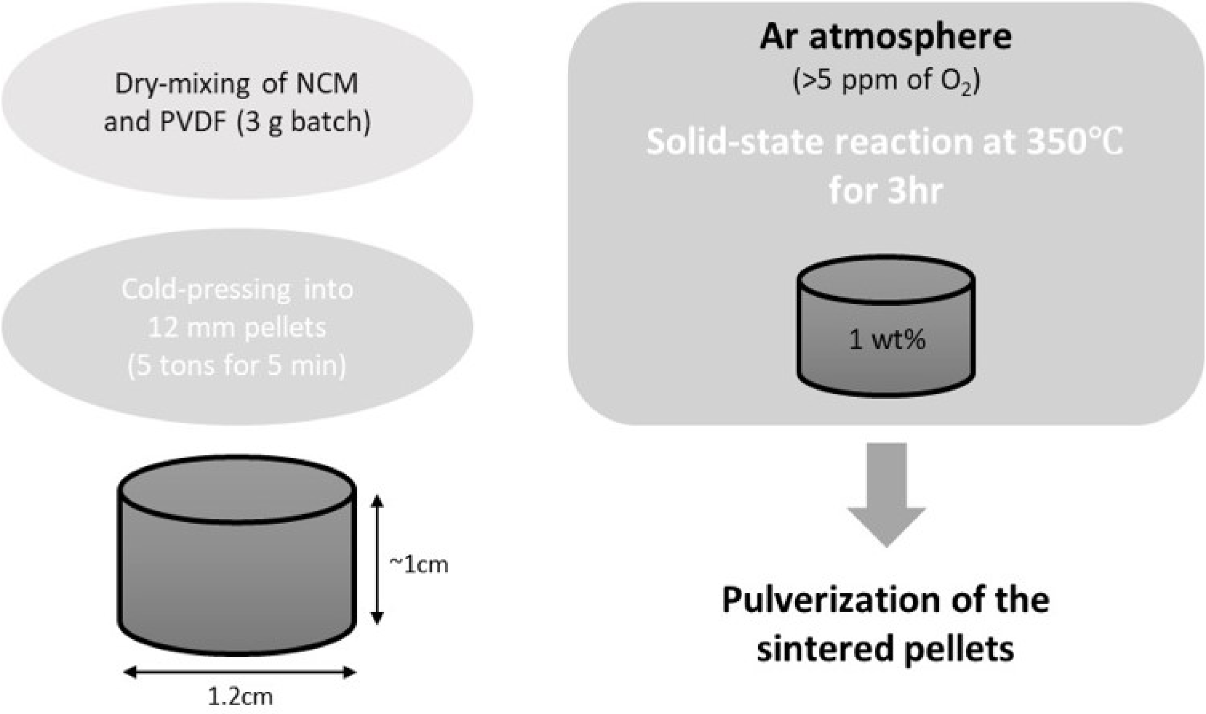

Fig. S1 Schematic illustration of the F-coating process applied to high-Ni NCM using PVDF decomposition under an argon atmosphere.

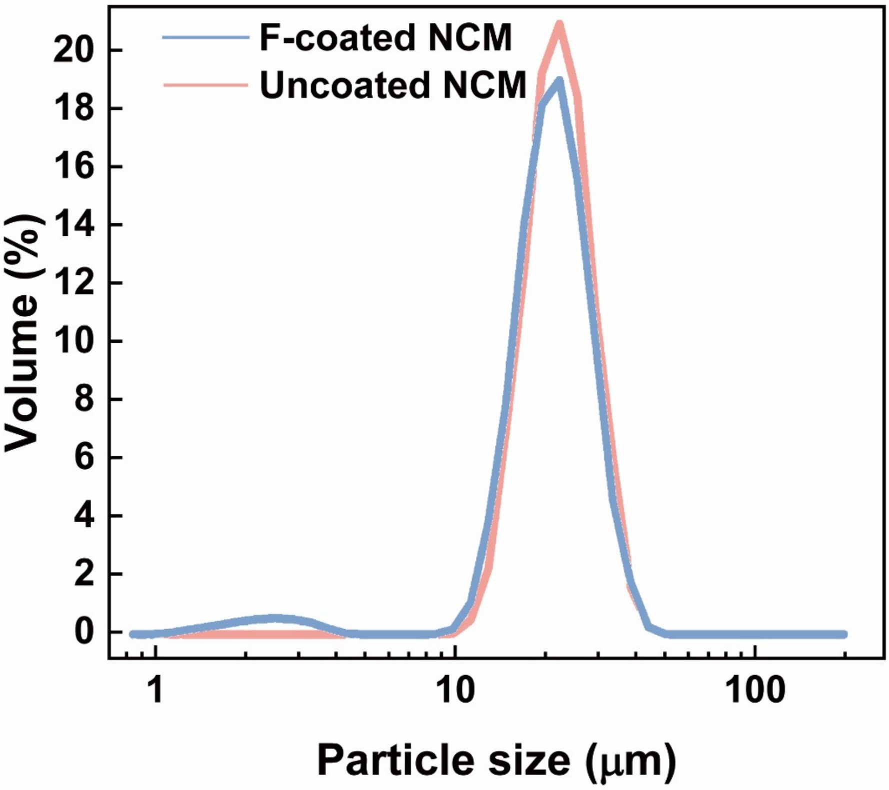

Fig. S2 Diameter distributions of uncoated and F-coated NCMs measured through particle size analyzer (PSA, Mastersize2000, Malvern Panalytical) with 2000 rpm and ultrasonic dispersion.

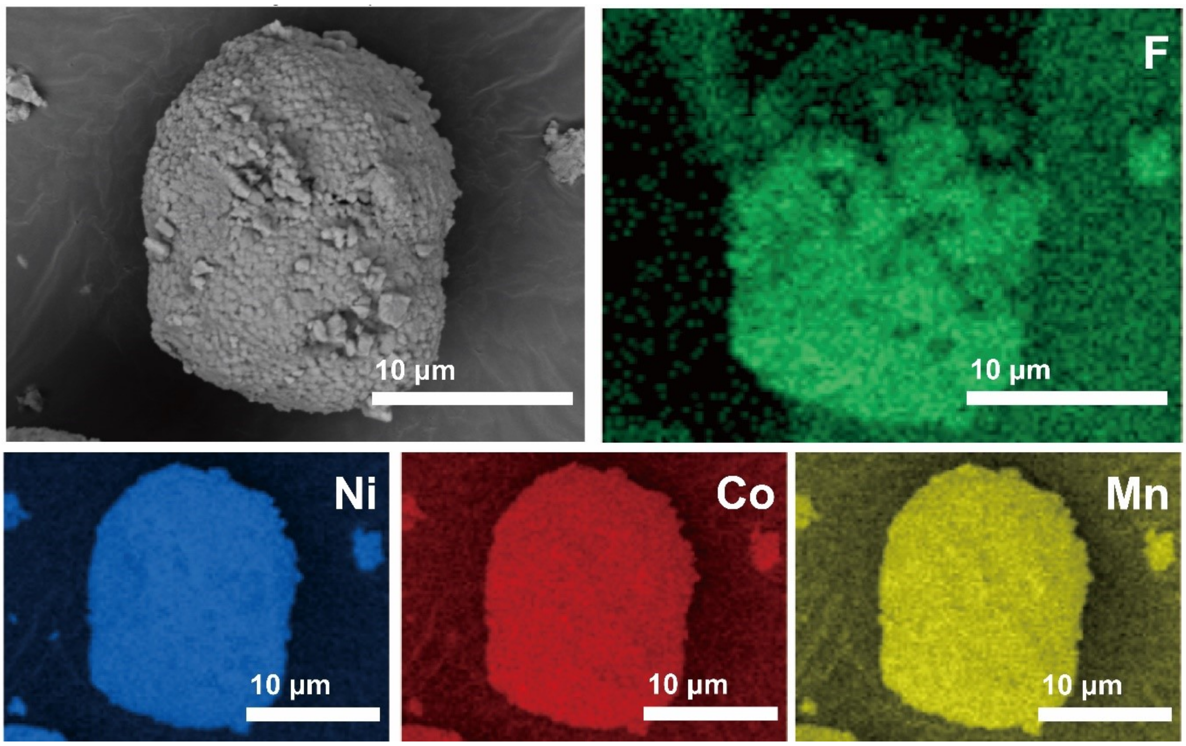

Fig. S3 SEM image and EDS elemental maps of F-coated NCM particle.

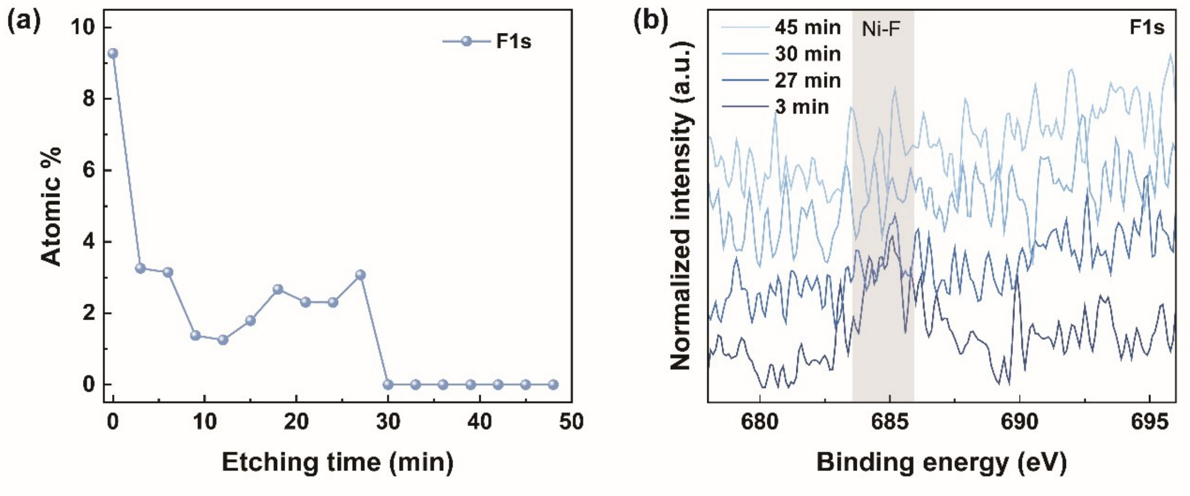

Fig. S4 (a) Atomic ratio estimated from the F 1*s* XPS spectra as a function of the Ar-ion etching time. **(b)** F 1*s* spectra at various etching times (e.g., 3, 27, 30 and 45 min). The gray shaded area indicates the binding energy region of Ni-F bonding.

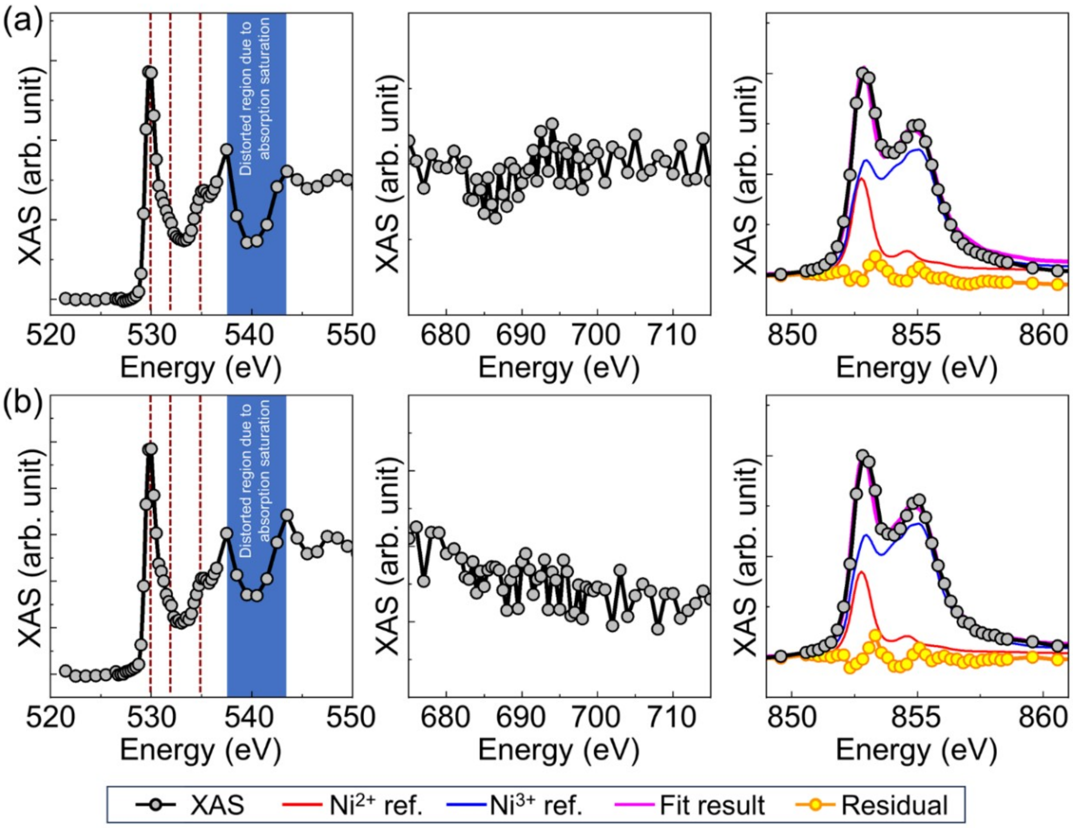

Fig. S5 (a) Averaged and **(b)** single-pixel XAS spectra across the O *K*-, F *K*-, and Ni L_3-edges. The region used for averaging and the position of the selected pixel are indicated in **Fig. 2**. The O *K*-edge spectra near 540 eV are distorted due to saturation effects mainly arising from detector nonlinearity. Further discussion of the saturation effects can be found in the literature [10, 11]. The Ni L_3-edge spectra are simulated using a linear combination of Ni^{2+} and Ni^{3+} reference spectra by a least-squares minimization method under non-negative constraints. The residual indicates the difference between the fitted and measured XAS spectra.

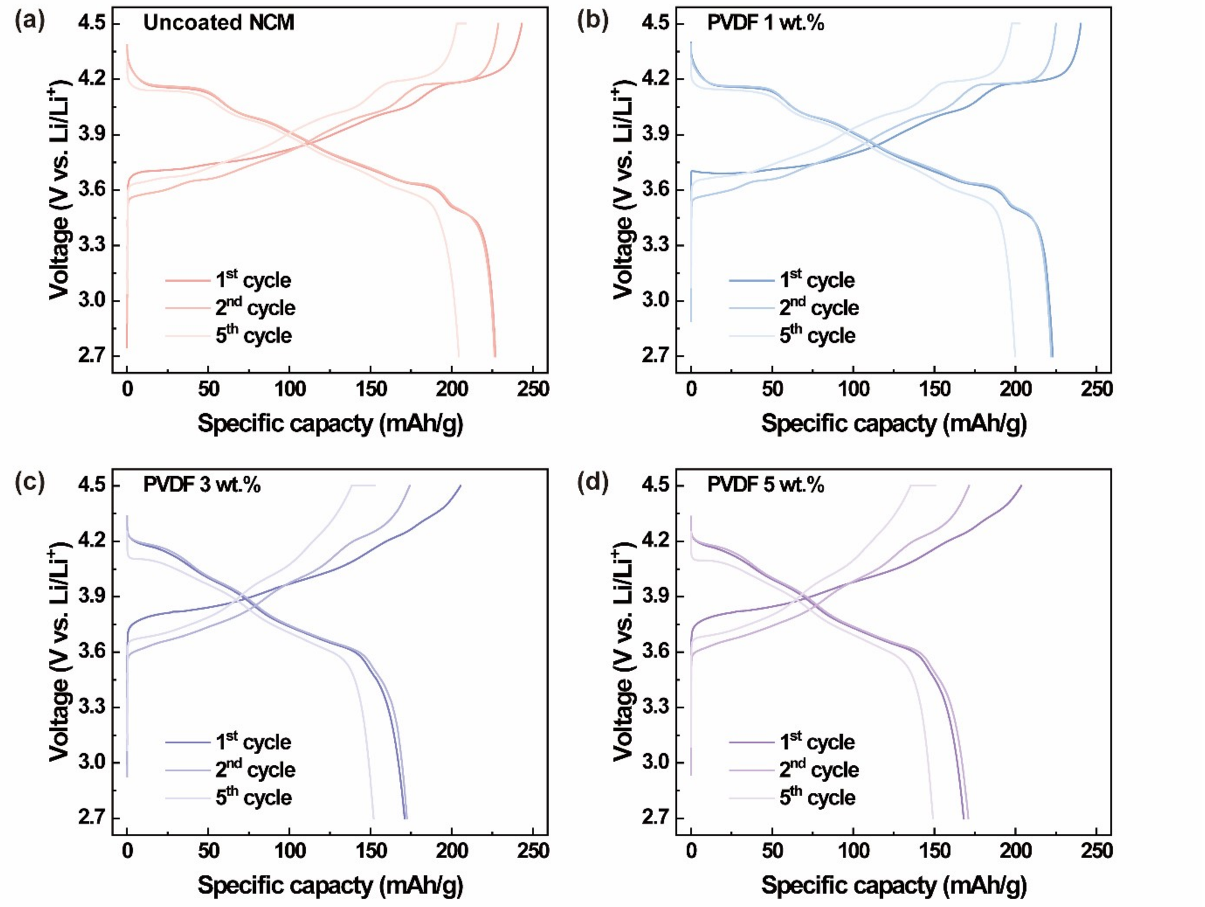

Fig. S6 Voltage profiles of NCM samples with varying PVDF coating contents (1, 3, and 5 wt.%) and the uncoated sample, measured within a potential window of 2.7-4.5 V.

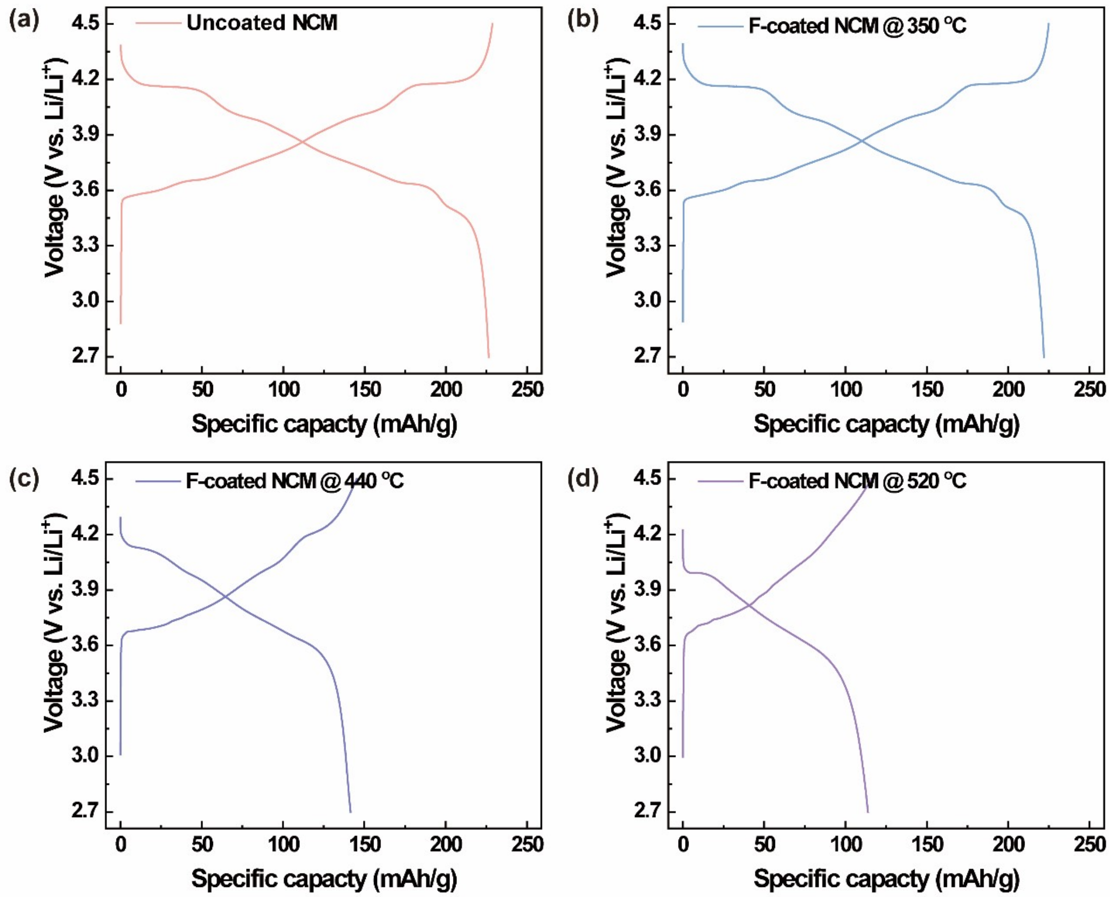

Fig. S7 Voltage profiles of F-coated NCM samples prepared at different annealing temperatures (350, 440, and 520 °C) compared to the uncoated sample, measured within a potential window of 2.7-4.5 V.

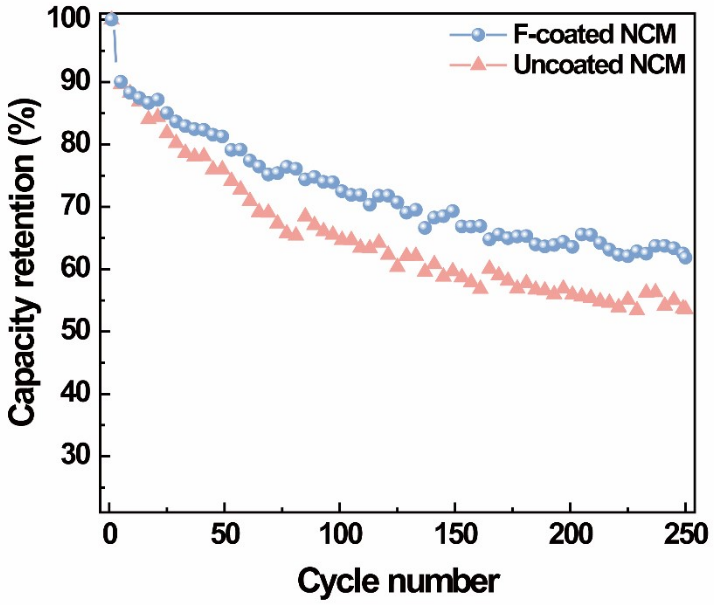

Fig. S8 Cycling performance of uncoated and F-coated NCM cells at room temperature within a potential window of 2.7-4.5 V.

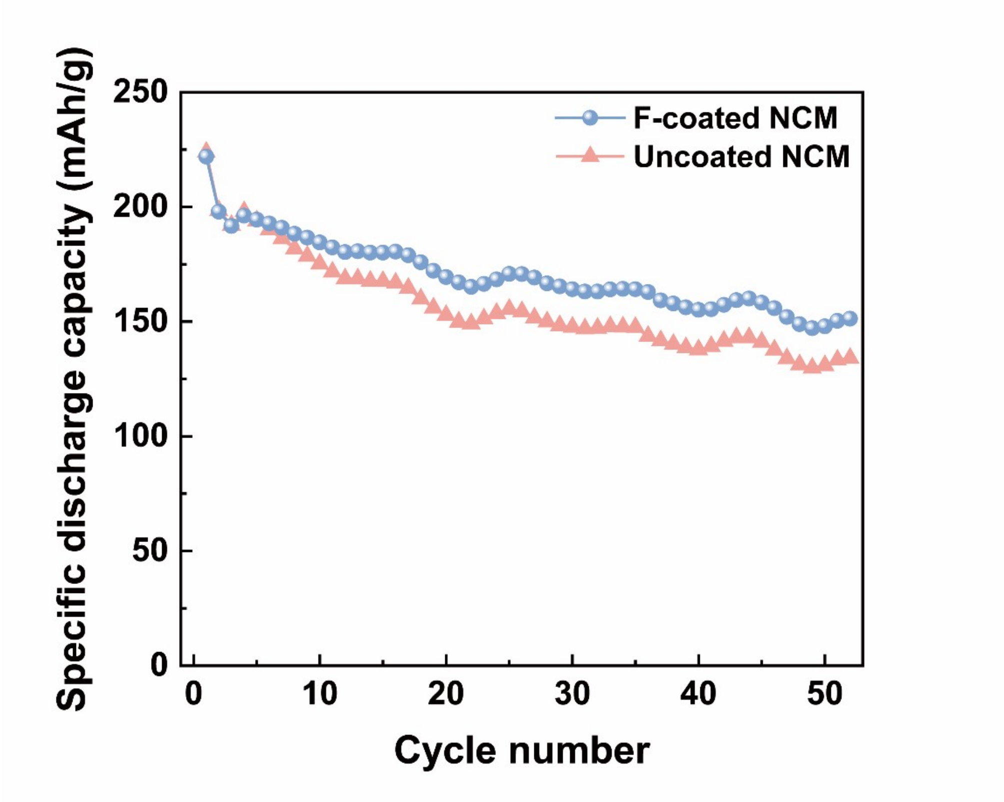

Fig. S9 Cycling performance of uncoated and F-coated NCM cells at under controlled charge-capacity conditions to exclude the influence of different initial delithiation levels.

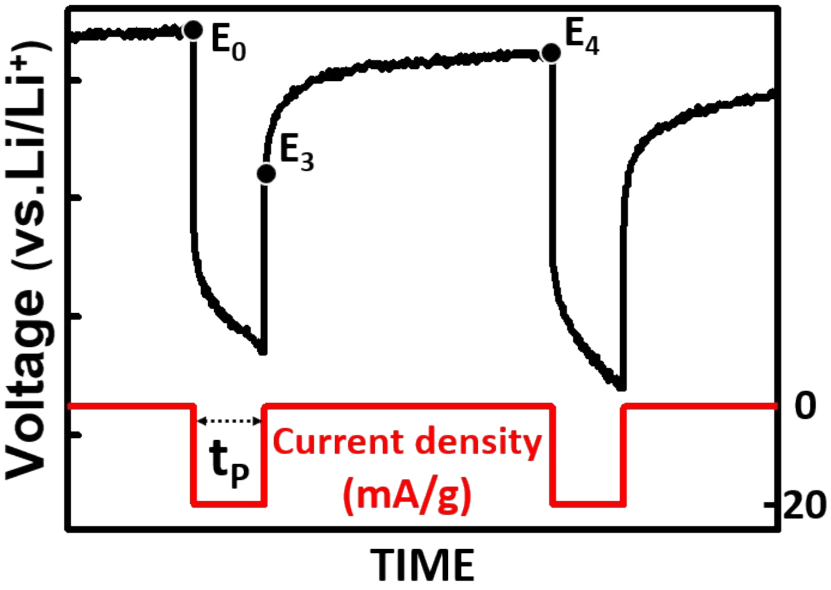

Fig. S10 Schematic of the GITT protocol and calculation of Li$^+$ diffusivity. E_0 is the equilibrium potential before the current pulse, E_3 is the potential at the end of the current pulse (excluding the instantaneous iR drop), and E_4 is the quasi-equilibrium potential after relaxation.

Li ratio (%)	**Uncoated NCM**				**F-coated NCM**			
	1	2	3	Average	1	2	3	Average
Li_2CO_3	2.216	2.346	2.285	2.282	2.545	2.323	2.589	2.486
$LiOH\cdot H_2O$	0.568	0.441	0.549	0.519	0.185	0.234	0.178	0.199
Total	2.784	2.787	2.834	2.801	2.730	2.567	2.767	2.685

Table S1. Residual lithium titration results of uncoated and F-coated NCM**.**

[1] A. Nickol, T. Schied, C. Heubner, M. Schneider, A. Michaelis, M. Bobeth, G. Cuniberti, Journal of The Electrochemical Society, 167 (2020).

[2] T. Feggeler, A. Levitan, M.A. Marcus, H. Ohldag, D.A. Shapiro, Journal of Electron Spectroscopy and Related Phenomena, 267 (2023) 147381.

[3] P.M. Csernica, S.S. Kalirai, W.E. Gent, K. Lim, Y.-S. Yu, Y. Liu, S.-J. Ahn, E. Kaeli, X. Xu, K.H. Stone, A.F. Marshall, R. Sinclair, D.A. Shapiro, M.F. Toney, W.C. Chueh, Nature Energy, 6 (2021) 642-652.

[4] B.L. Henke, E.M. Gullikson, J.C. Davis, Atomic Data and Nuclear Data Tables, 54 (1993) 181-342.

[5] Y.-S. Yu, M. Farmand, C. Kim, Y. Liu, C.P. Grey, F.C. Strobridge, T. Tyliszczak, R. Celestre, P. Denes, J. Joseph, H. Krishnan, F.R.N.C. Maia, A.L.D. Kilcoyne, S. Marchesini, T.P.C. Leite, T. Warwick, H. Padmore, J. Cabana, D.A. Shapiro, Nature Communications, 9 (2018) 921.

[6] K.Y. Chung, W.-S. Yoon, K.-B. Kim, B.-W. Cho, X.-Q. Yang, Journal of Applied Electrochemistry, 41 (2011) 1295-1299.

[7] M. Sina, R. Thorpe, S. Rangan, N. Pereira, R.A. Bartynski, G.G. Amatucci, F. Cosandey, The Journal of Physical Chemistry C, 119 (2015) 9762-9773.

[8] H.-J. Shin, N. Kim, H.-S. Kim, W.-W. Lee, C.-S. Lee, B. Kim, Journal of Synchrotron Radiation, 25 (2018) 878-884.

[9] N. Otsu, IEEE Transactions on Systems, Man, and Cybernetics, 9 (1979) 62-66.

[10] S. Hanhan, A.M. Smith, M. Obst, A.P. Hitchcock, Journal of Electron Spectroscopy and Related Phenomena, 173 (2009) 44-49.

[11] M.A. Marcus, Journal of Electron Spectroscopy and Related Phenomena, 264 (2023) 147310.